RSC Advances

PAPER

View Article Online
View Journal | View Issue

Cite this: *RSC Adv.*, 2025, **15**, 15763

Star-shaped small-molecule hole-transport materials for dopant-free perovskite solar cells†

Ilya V. Martynov, *[a] Mariia M. Agapitova,[bc] Ilya E. Kuznetsov,[b] Valentyn S. Volkov,[d] Marina Tepliakova,[c] Alexander V. Akkuratov[b] and Aleksey V. Arsenin[ae]

Perovskite solar cells hold great potential for efficient photovoltaics, with hole-transporting materials being key to their success. We synthesized three new conjugated small-molecule HTMs—**DPAMes-TT**, **TPA-TT**, and **PhFF-TT**—and evaluated them in n–i–p PSCs. These molecules, featuring triphenylamine or trifluorobenzene cores, were analyzed in terms of their optical, electrochemical, thermal, and charge transport properties. **DPAMes-TT** and **TPA-TT** exhibited narrow bandgaps (2.66 eV and 2.61 eV), HOMO levels well-aligned with $MAPbI_3$'s valence band (−5.28 eV and −5.30 eV *vs.* −5.4 eV), and high hole mobilities. In contrast, **PhFF-TT** with trifluorobenzene core had a wider bandgap (2.95 eV), a less favorable HOMO (−5.14 eV), and signs of J-aggregation, impairing charge transport. PSCs with **DPAMes-TT** delivered the highest efficiency (19.3%), outperforming **TPA-TT** (18.5%) and the PTAA reference (18.1%). **PhFF-TT** devices, however, reached only 12.6% limited by recombination and poor interface quality, as revealed by photoluminescence. Charge transport studies confirmed **DPAMes-TT**'s superior hole extraction, while **PhFF-TT** suffered higher recombination losses. These findings show how molecular design shapes PSC performance, with amine-based HTMs like **DPAMes-TT** and **TPA-TT** excelling over trifluorobenzene-based HTMs.

Received 9th April 2025
Accepted 1st May 2025

DOI: 10.1039/d5ra02466h

rsc.li/rsc-advances

Introduction

Perovskite solar cell (PSC) research has rapidly advanced over the past decade, now exceeding 26% in power conversion efficiency, positioning them as a serious contender for conventional silicon-based technologies.[1,2] This remarkable progress stems from the unique properties of perovskite materials, including strong light absorption, long charge carrier diffusion lengths, and tunable bandgaps, making them a promising option for cost-effective and high-performance solar energy solutions.[3,4] A key component in PSCs is the hole-transporting material (HTM), which plays an essential role in extracting photogenerated holes from the perovskite layer, reducing recombination losses, and ensuring efficient charge transport to the electrode.

Traditional HTMs such as Spiro-OMeTAD, PTAA, and conjugated polymers provide high efficiencies yet exhibit key limitations.[5–9] These materials often require complex synthesis, need dopants like Li-TFSI to boost conductivity, and suffer from poor long-term stability due to sensitivity to moisture, oxygen, and heat.[10–12] Dopants further complicate large-scale production by increasing costs and introducing degradation pathways, limiting the commercial potential of PSCs. Recent efforts have shifted toward developing dopant-free small-molecule HTMs that can offer comparable performance while improving stability and reducing costs.[13–17] Small molecules, particularly those based on triphenylamine with π-spacers, have shown promise due to their extended π-conjugation, which enhances charge transport, and their structural flexibility, allowing fine-tuning of optoelectronic properties through substituent modifications.[18–21] Recent research has demonstrated that highly ordered molecular packing is typically responsible for the high charge mobility of small-molecule hole-transporting materials.[22–24]

This study introduces a novel class of star-shaped, dopant-free small-molecule HTMs—**DPAMes-TT**, **TPA-TT**, and **PhFF-TT**—designed to enhance the efficiency and stability of perovskite solar cells. The innovation lies in leveraging the star-shaped architecture to promote π–π stacking and film crystallinity, enabling high efficiency (19.3% for **DPAMes-TT**) and improved stability (more 90% retention after 1200 hours), without the use of dopants. Unlike conventional HTMs like

[a]*Moscow Center for Advanced Studies, Kulakova Str. 20, 123592, Moscow, Russia. E-mail: martinov@mitht.org*
[b]*Federal Research Center of Problems of Chemical Physics and Medicinal Chemistry, Russian Academy of Sciences. FRC PCPMC RAS, Academician Semenov Avenue 1, Chernogolovka, 142432, Moscow Region, Russian Federation*
[c]*Skolkovo Institute of Science and Technology, 3 Nobel Str., 143026, Moscow, Russian Federation*
[d]*Emerging Technologies Research Center, XPANCEO, Internet City, Emmay Tower, Dubai, United Arab Emirates*
[e]*Laboratory of Advanced Functional Materials, Yerevan State University, 0025, Yerevan, Armenia*

† Electronic supplementary information (ESI) available. See DOI: https://doi.org/10.1039/d5ra02466h

PTAA, which often require dopants that compromise stability, our approach offers a cost-effective and stable alternative, addressing key challenges in PSC commercialization while maintaining competitive performance.

Results and discussion

The chemical structures of new materials **TPA-TT**, **PhFF-TT**, and **DPAMes-TT** and their synthesis are illustrated in Fig. 1. We started with the three-step synthesis of triisopropyl(5′-(trimethylstannyl)-[2,2′-bithiophen]-5-yl)silane (**3**). First, 2,2′-bithiophene was obtained *via* Kumadu cross-coupling reaction between 2-bromothiophene and thiophen-2-yl magnesium bromide. Then, compound **1** was lithiated with *n*-butyllithium and quenched with chlorotriisopropylsilane. Compound **3** was synthesized similarly from compound **2**, *n*-butyllithium and trimethylchlorostannane. The small molecules **TPA-TT**, **PhFF-TT**, and **DPAMes-TT** were prepared by Stille reaction between compound **3** and tris(4-bromophenyl)amine, 1,3,5-tribromo-2,4,6-trifluorobenzene, *N*,*N*-bis(4-bromophenyl)-2,4,6-trimethylaniline, respectively.

The thermal properties of the synthesized hole-transporting materials were evaluated using thermogravimetric analysis (TGA) and differential scanning calorimetry (DSC). The TGA data reveal that all materials exhibit high thermal stability, with a 5% mass loss occurring above 470 °C – specifically at 487 °C, 485 °C, and 477 °C for **DPAMes-TT**, **TPA-TT**, and **PhFF-TT**, respectively (see Fig. 2b). Analysis of the DSC heating curves shows distinct endothermic peaks, corresponding to the melting phase transitions of the materials.

Notably, **PhFF-TT** displays two T_m values (70 °C and 157 °C), indicative of polymorphic behavior stemming from its trifluorobenzene core and molecular packing variations. The lower T_m corresponds to a less stable polymorph, while the higher T_m reflects the dominant crystalline phase.

The optical properties of the small molecules were investigated in dichloromethane solution and in thin films. As presented in Fig. 2a and in Table 1, all materials in solution display narrow absorption bands with absorption maximum at 415 nm, 410 nm, and 358 nm, corresponding to the violet and near-ultraviolet regions of the spectrum. Additionally, pronounced shoulders are observed in the short-wavelength region that might be attributed to the formation of H-aggregates. Specifically, **DPAMes-TT** and **TPA-TT** exhibit stronger intermolecular interactions, whereas **PhFF-TT** shows no clear evidence of aggregation in solution.[25] In contrast, UV-visible spectra of thin films reveal distinct changes. For **DPAMes-TT** and **TPA-TT**, the absorption maxima undergo a hypsochromic shift to 406 nm and 408 nm, respectively, suggesting the H-aggregation in the solid state. Conversely, **PhFF-TT** exhibits signs of J-aggregation, characterized by a broadening band and a bathochromic shift to 364 nm.[26,27]

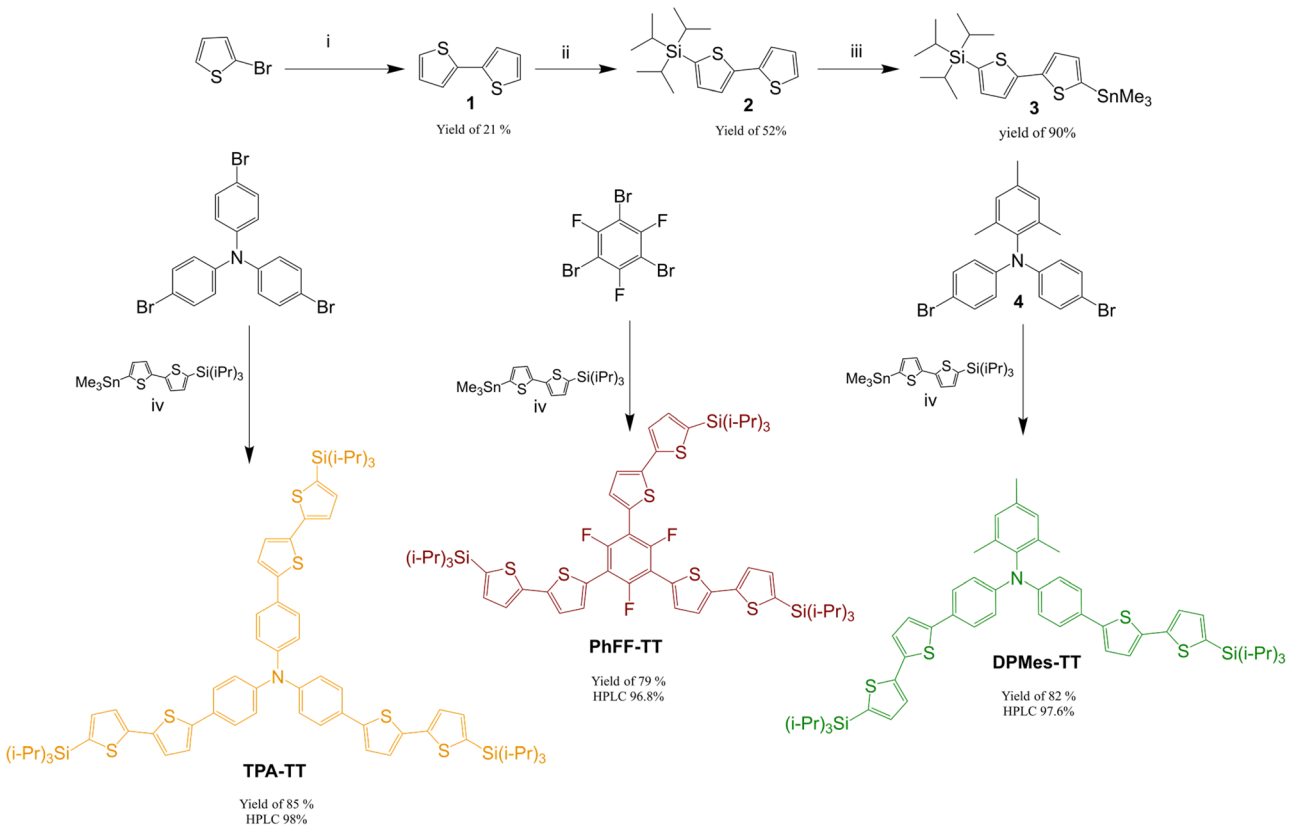

Fig. 1 Synthesis of small molecule HTMs. Conditions: **i** – THF, thiophen-2-yl magnesium bromide, $Ni(dppp)Cl_2$; **ii** – THF, BuLi, $(i\text{-}Pr)_3SiCl$; **iii** – THF, BuLi, Me_3SnCl; **iv** – DMF, $Pd(OAc)_2$,PPh_3.

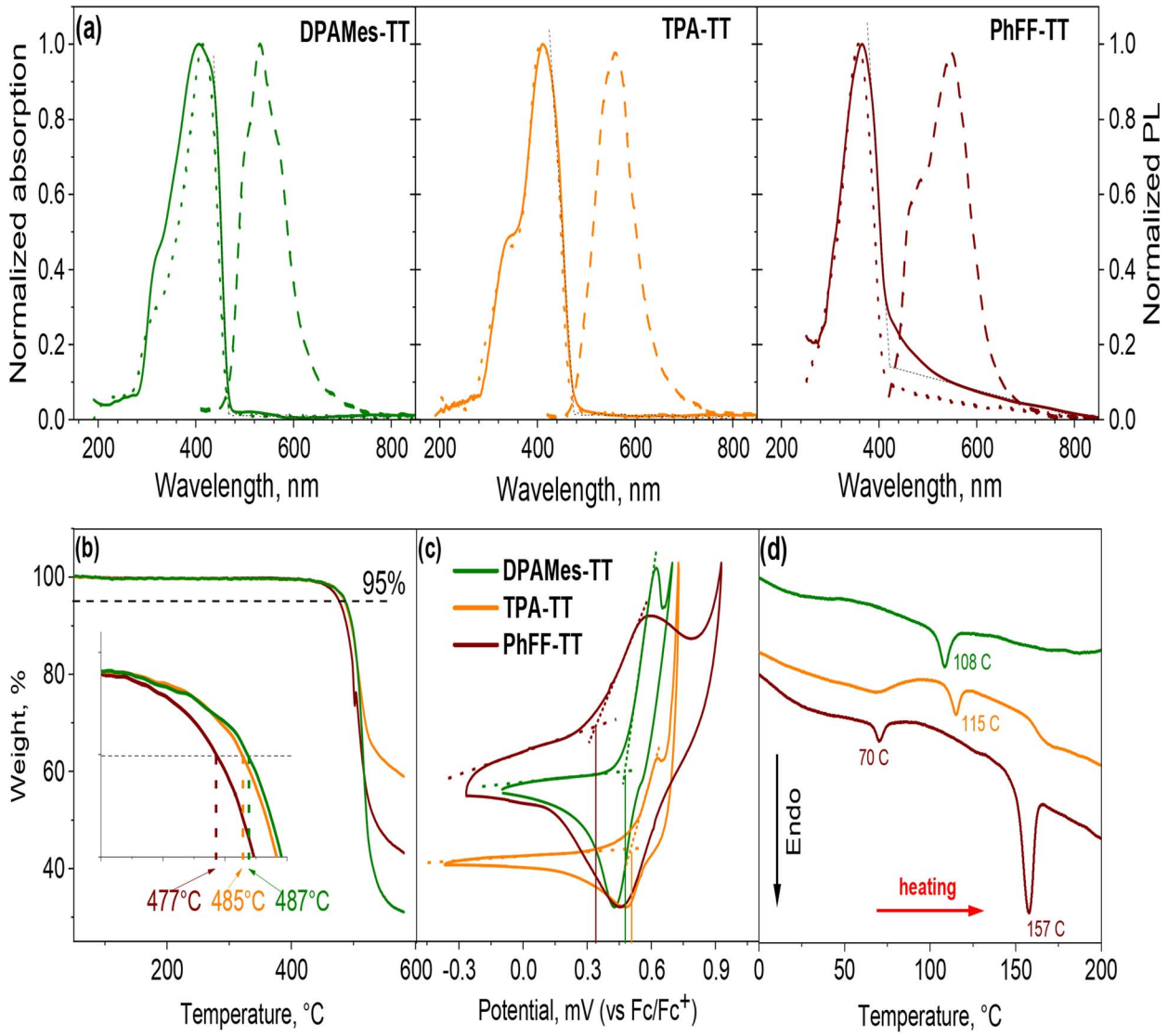

Fig. 2 (a) UV-visible absorption spectra of **DPAMes-TT** (green), **TPA-TT** (orange), and **PhFF-TT** (red) in dichloromethane solution (doted lines) and in thin films (solid lines), and photoluminescence (PL) spectra in thin films (dashed lines); (b) TGA curves; (c) cyclic voltammetry (CV) curves; (d) differential scanning calorimetry (DSC) heating curves.

Photoluminescence spectra of thin films prepared from materials exhibit extremely weak emission intensities for **DPAMes-TT** and **TPA-TT**, with maxima at 532 nm and 560 nm, respectively (Fig. S1†). These spectra show Stokes shifts of 126 nm and 152 nm, respectively, indicating enhanced exciton interactions between the π-systems of the molecules. This suggests energy-level splitting in the excited state, where the energy increases and low-energy radiative recombination is suppressed. In contrast, **PhFF-TT** displays a more significant red-shift in its PL band, with a Stokes shift of 181 nm. This shift likely arises from J-aggregation in the thin films, as evidenced by an increase in emission intensity and a redistribution of

Table 1 Optical, electrochemical, and thermal properties of the HTMs **DPAMes-TT**, **TPA-TT**, and **PhFF-TT**

HTM	$ABS_{max}^{sol/film}$,[a] [nm]	PL_{max}^{film}, [nm]	$\lambda_{onset}/\lambda_{int}$, [nm]	E_g^{opt},[b] [eV]	E_{onset}^{ox}, [V *vs.* Fc^+/Fc]	HOMO,[c] [eV]	LUMO,[d] [eV]	T_d, [°C]	T_m, [°C]
DPAMes-TT	415/406	532	466/466	2.66	0.48	−5.28	−2.62	487	108
TPA-TT	410/408	560	475/475	2.61	0.50	−5.30	−2.69	485	115
PhFF-TT	358/364	545	421/442	2.95	0.34	−5.14	−2.19	477	70; 157

[a] Absorption maxima of the UV-vis spectra in solution and thin film. [b] Optical bandgap determined by $E_g^{opt} = 1240/\lambda_{onset}$. [c] $E_{HOMO} = -(E_{onset}^{ox}$ *vs.* $Fc/Fc^+ + 4.8)$, eV. [d] LUMO is calculated from HOMO energy levels and optical band gaps.

spectral peaks at 475 nm and 545 nm, with a marked preference for the longer-wavelength region.[28,29]

The high degree of aggregation in both solutions and films complicates the determination of the optical bandgap. As shown in Table 1, for molecules with H-aggregation (**DPAMes - TT** and **TPA-TT**), the absorption onset (λ-onset) and the intersection of absorption and photoluminescence spectra (λ-int) are nearly identical, at 466 nm and 475 nm, respectively. In contrast, for **PhFF-TT**, which exhibits J-aggregation, these values diverge significantly, with λ-onset at 421 nm and λ-int at 442 nm. To achieve consistent and comparable results across all materials in solution, we taken the λ-onset values. Consequently, the optical bandgaps are calculated as 2.66 eV, 2.61 eV, and 2.95 eV for **DPAMes-TT**, **TPA-TT**, and **PhFF-TT**, respectively. The values of E_g reflect the differences in chemical structures of the materials. **DPAMes-TT** and **TPA-TT**, featuring electron-donating triphenylamine and mesityl groups, respectively, conjugated to a bithiophene core, enhance π-electron delocalization, lowering the bandgap. Conversely, **PhFF-TT** incorporates an electron-withdrawing trifluorobenzene core, which reduces conjugation due to steric effects, resulting in a wider bandgap. The substituent effects also influence aggregation tendencies, further modulating the optical properties observed.

Cyclic voltammetry was employed to assess the electrochemical properties of the materials, as shown in Fig. 2c. All three hole-transporting materials exhibit quasi-reversible oxidation waves. The HOMO energy levels were determined using the onset of oxidation potential (E_{onset}^{ox}), measured relative to the ferrocene/ferrocenium (Fc/Fc^+) redox couple, and calculated according the equation $E_{HOMO} = -(E_{onset}^{ox}$ *vs.* $Fc/Fc^+ + 4.8)$ eV.[30] This yielded HOMO values of −5.28 eV, −5.30 eV, and −5.14 eV for **DPAMes-TT**, **TPA-TT**, and **PhFF-TT**, respectively. The deep-lying HOMO levels of **DPAMes-TT** and **TPA-TT** align good with VB of $MAPbI_3$ (−5.43 eV), which should enhance the open-circuit voltage by reducing energy losses. In contrast, the higher HOMO of **PhFF - TT** may stem from its J-aggregation tendencies. Using the optical bandgaps (E_g), the LUMO energy levels were calculated as $E_{LUMO} = E_{HOMO} + E_g$, resulting −2.62 eV, −2.69 eV, and −2.19 eV for **DPAMes-TT**, **TPA-TT**, and **PhFF-TT**, respectively. The energy levels diagram for all materials used in the devices is presented in Fig. 3a.

Following a comprehensive characterization of their physicochemical properties, **DPAMes-TT** and **TPA-TT** emerged as promising candidates, displaying attributes suggestive of superior performance as hole-transporting materials. On the contrary, **PhFF-TT** was found to be significantly less effective, which is explained by the replacement of its central functional element with an electron acceptor trifluorobenzene fragment, which can reduce coupling and affect charge transfer.

To test this hypothesis, photovoltaic devices were fabricated using an n–i–p architecture ($ITO/SnO_2/PCBA/MAPbI_3/HTM/MoO_x/Ag$), with **DPAMes-TT**, **TPA-TT**, and **PhFF-TT** employed as HTMs. A reference HTM, prepared using commercially available PTAA, was included for comparative analysis. The energy level diagram (Fig. 3a) confirms that the HOMO levels of **DPAMes-TT** and **TPA-TT** align closely with that of **$MAPbI_3$**, facilitating efficient hole extraction, while **PhFF-TT**'s higher HOMO gives a larger energy offset. The photovoltaic parameters of these devices are summarized in Table 2, and current–voltage (*J–V*) characteristics are shown in Fig. 3b. Devices incorporating **DPAMes-TT** provided the highest power conversion efficiency, with a maximum of 19.3%, surpassing both its counterparts and the reference maximum PCE of 18.1%. **TPA-TT**-based devices also demonstrated good performance, with a PCE_{max} of 18.5%, slightly outperforming **PTAA**. In contrast, **PhFF-TT**-based devices showed the lowest PCE_{max} of 12.6%, reflecting significant variability and poor performance, consistent with its optical and electrochemical properties. These results compare favorably with the best devices using $MAPbI_3$ and other TPA derivatives.[31–34]

Focusing on individual parameters, **DPAMes-TT** and **TPA-TT** devices exhibited high open-circuit voltages (V_{oc}) with maximum values of 1040 mV each (averages of 1020 ± 20 mV and 1040 ± 20 mV, respectively), compared to PTAA's maximum of 1020 mV. This originated from good alignment of HOMO of **DPAMes-TT** and **TPA-TT** with VB of $MAPbI_3$ and minimized energy losses at the interface. **PhFF-TT**, however, showed a lower V_{oc} with a maximum of 980 mV, reflecting greater energy loss due to its HOMO mismatch. The short-circuit current densities (J_{sc}) were also superior for **DPAMes-TT** and **TPA-TT**, with maximum values of 23.9 mA cm^{-2} and 23.6 mA cm^{-2}, respectively as compared to J_{sc} of solar cells with **PTAA** – 22.8 mA cm^{-2}. **PhFF-TT** J_{sc} was comparable at a maximum of 22.8 mA

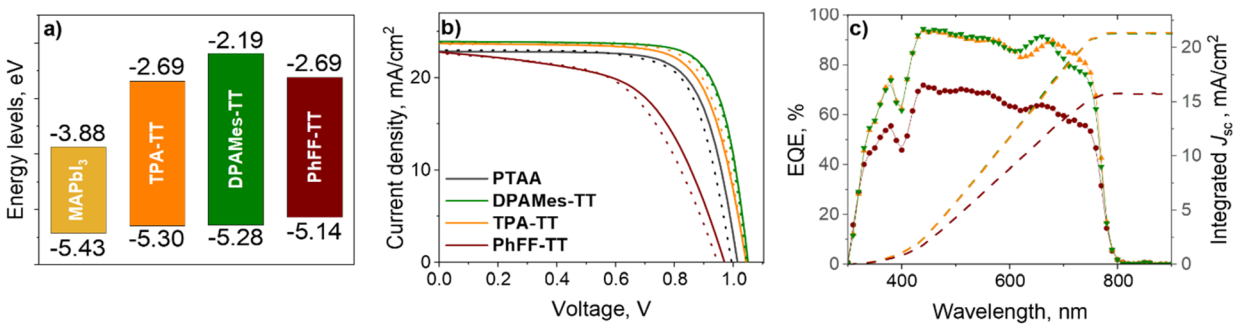

Fig. 3 (a) Energy levels diagram, (b) *J–V* characteristics, and (c) EQE spectra of perovskite solar cells with DPAMes-TT, TPA-TT, PhFF-TT, and PTAA as HTMs.

Table 2 Photovoltaic parameters of perovskite solar cells with different HTMs in the configuration ITO/SnO_2/PCBA/$MAPbI_3$/HTM/MoO_x/Ag: maximum (average ± standard deviation)

M	V_{oc}, [mV]	J_{sc}, [mA cm^{-2}]	FF, [%]	PCE, [%]	R_s, [Ω]	R_{sh}, [Ω]
DPAMes-TT	1040 (1020 ± 20)	23.9 (22.9 ± 0.9)	77.7 (75.8 ± 2)	19.3 (18.2 ± 1.1)	1.25 ± 4.6 × 10^{-3}	1101 ± 110
TPA-TT	1040 (1040 ± 20)	23.6 (23.1 ± 0.7)	75.3 (73.5 ± 1)	18.5 (17.6 ± 0.9)	2.75 ± 4.0 × 10^{-2}	1120 ± 108
PhFF-TT	980 (930 ± 50)	22.8 (20.4 ± 1.4)	56.2 (52.0 ± 5)	12.6 (9.8 ± 2.8)	6.21 ± 1.1 × 10^{-1}	183 ± 13
PTAA	1020 (1000 ± 20)	22.8 (22.6 ± 0.6)	77.8 (75.6 ± 3)	18.1 (17.1 ± 1.2)	3.86 ± 6.5 × 10^{-2}	1006 ± 174

cm^{-2} but dropped significantly in average (20.4 ± 1.4 mA cm^{-2}), indicating inconsistency. These J_{sc} values were corroborated by the EQE spectra (Fig. 3c). The integrated J_{sc} values closely match the experimental for **DPAMes-TT**, **TPA-TT**, and **PTAA**. However, **PhFF-TT**-based devices showed discrepancies, likely due to poor HTL/$MAPbI_3$ interface quality, as evidenced by their low fill factor (FF) of 56.2%. In contrast, **DPAMes-TT** and **TPA-TT** achieved high FF values of 77.7% and 75.3%, respectively, comparable to **PTAA** 77.8%, indicating efficient charge extraction and minimal recombination losses. The EQE spectra further highlight performance differences: EQE values for **DPAMes-TT** and **TPA-TT**remain above 80% across the 400–750 nm range, reflecting their strong spectral response, while **PhFF-TT** EQE drops below 70% beyond 600 nm, consistent with its wider bandgap (2.95 eV, λ-onset 421 nm) and reduced absorption in the red region. Additionally, the series resistance (R_s) and shunt resistance (R_{sh}) values from Table 2 provide insight into device quality. **DPAMes-TT** and **TPA-TT** exhibit low R_s (1.25 ± 0.0046 Ω and 2.75 ± 0.04 Ω) and high R_{sh} (1101 ± 110 Ω and 1120 ± 108 Ω), supporting their high FF and efficient charge transport. Conversely, **PhFF-TT** higher R_s (6.21 ± 0.11 Ω) and significantly lower R_{sh} (183 ± 13 Ω) indicate increased recombination and leakage currents, further explaining its poor FF and PCE. **PTAA** R_s (3.86 ± 0.065 Ω) and R_{sh} (1006 ± 174 Ω) are intermediate, consistent with its balanced but slightly lower performance compared to **DPAMes-TT** and **TPA-TT**.[35] These results underscore the influence of chemical structure on device performance. The electron-donating groups in **DPAMes-TT** and **TPA-TT** enhance conjugation, improve energy level alignment, and promote H-aggregation, leading to superior charge transport and interface compatibility. In contrast, **PhFF-TT**'s trifluorobenzene core induces J-aggregation, and exacerbates energy mismatch and interfacial defects, limiting its efficiency.

To gain detail insight into the recombination processes occurring within the device, both in the hole-transporting material layer and at the HTM/perovskite interface, we conducted a series of experiments. The charge transport properties of the synthesized small molecules were investigated to evaluate their potential as HTMs. Hole mobilities were measured using the space-charge-limited current method in hole-only devices with the architecture ITO/PEDOT:PSS/HTM/MoO_x/Ag.[36,37] The *J–V* curves for these devices, incorporating the new HTMs, are presented in Fig. 4a, confirming the calculated hole mobilities for **DPAMes-TT**, **TPA-TT**, and **PhFF-TT** as 8.7 × 10^{-4} cm^2 V^{-1} s^{-1}, 2.7 × 10^{-4} cm^2 V^{-1} s^{-1}, and 2.1 × 10^{-4} cm^2 V^{-1} s^{-1}, respectively. These values are higher than that of **PTAA**, which typically exhibits a hole mobility of around 2 × 10^{-4} cm^2 V^{-1} s^{-1}.[5,38] The exceptionally high mobility of **DPAMes-TT** may be attributed to the high crystallinity of its films thereby enhancing mobility through strong intermolecular π–π interactions. In contrast, the lower mobility of **TPA-TT**, despite its H-aggregation, suggests a slightly less ordered film structure, potentially due to the bulkier triphenylamine unit. Similarly, **PhFF-TT** relatively low mobility, despite being higher than **PTAA**, can be linked to a more defective film structure, likely exacerbated by its J-aggregation tendencies, which disrupt efficient charge transport.[28]

To further assess the charge transport capacity and interfacial charge transfer dynamics of the three small-molecule HTMs, steady-state photoluminescence (PL) and time-resolved photoluminescence (TRPL) techniques were employed. Samples were prepared using the ITO/perovskite/HTM configuration, with ITO/perovskite ($MAPbI_3$) as the control. As illustrated in Fig. 4b, the steady-state PL spectra reveal significant quenching in the ITO/perovskite/**DPAMes-TT** sample, indicating superior charge extraction efficiency at the perovskite/

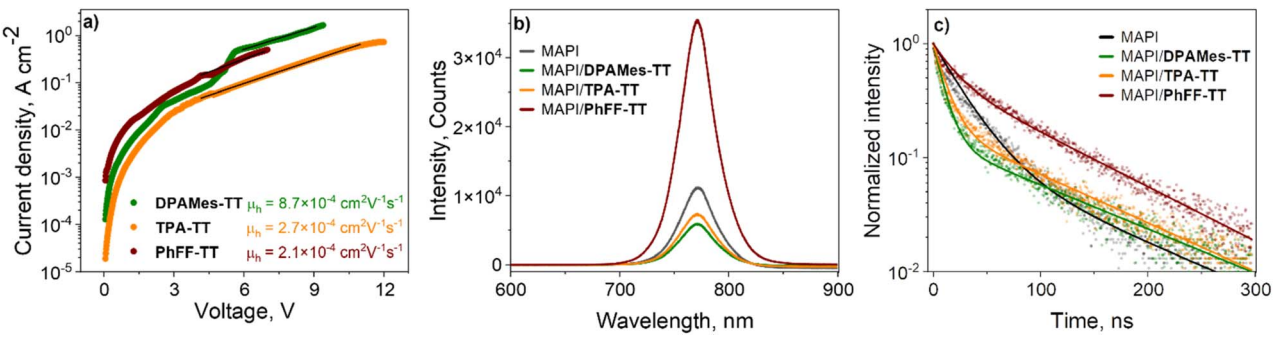

Fig. 4 (a) SCLC *J–V* Curves; (b) steady-state PL; (c) TRPL decay spectra, for perovskite/HTM bilayer films with DPAMes-TT, TPA-TT, PhFF-TT, and bare $MAPbI_3$ (MAPI).

DPAMes-TT interface compared to the other HTMs. **TPA-TT** also shows notable quenching, though less pronounced than **DPAMes-TT**, while the perovskite/**PhFF-TT** sample exhibits a marked increase in PL intensity, suggesting enhanced radiative recombination likely due to a high density of interface defects.[39] TRPL measurements on perovskite/HTM bilayer films provided further insight into hole transfer dynamics from the conduction band of the perovskite to the HOMO level of the HTM. The TRPL decay curves (Fig. 4b) were fitted with a bi-exponential decay model, yielding two lifetime components: the faster decay (τ_1) attributed to charge transfer from the perovskite to the HTM or parasitic Shockley–Read–Hall recombination, and the slower component (τ_2) ascribed to bimolecular recombination.[40,41] For the control ITO/perovskite film, a long carrier lifetime was observed ($\tau_1 = 25.1$ ns, $\tau_2 = 109.6$ ns). In contrast, the ITO/perovskite/**DPAMes-TT** film exhibited a significant reduction in τ_1 to 9.3 ns, with τ_2 remaining relatively unchanged at 112.5 ns, indicating efficient charge transfer at the perovskite/**DPAMes-TT** interface and a reduction in bimolecular recombination within both the perovskite and the HTM, likely due to **DPAMes-TT** high hole mobility. **TPA-TT** showed a moderate decrease in τ_1 (not specified but implied to be between **DPAMes-TT** and **PhFF-TT**), consistent with its intermediate mobility and charge extraction efficiency. However, the perovskite/**PhFF-TT** film displayed a less pronounced reduction in τ_1 (18.5 ns) and a noticeable decrease in τ_2 (91.1 ns), suggesting increased bimolecular recombination, which correlates with the observed rise in steady-state PL intensity and points to significant interfacial recombination losses.

The molecular design of HTMs, specifically star-shaped *versus* linear architectures, plays a critical role in determining PSC performance through its influence on charge transport, film morphology, and device efficiency. The star-shaped structure of **DPAMes-TT** and **TPA-TT**, featuring triphenylamine cores, enhances π–π stacking and film crystallinity. This leads to superior hole mobilities (8.7×10^{-4} cm^2 V^{-1} s^{-1} for **DPAMes-TT** *vs.* 5.2×10^{-4} cm^2 V^{-1} s^{-1} for PTAA) and efficiencies of 19.3% and 18.5%, respectively, compared to linear HTMs like PTAA (18.1%). Linear HTMs, such as thiophene-based derivatives, often exhibit planar conformations that enhance charge transport but can result in aggregation, compromising film uniformity and long-term stability. Recent advancements report linear HTMs achieving efficiencies above 20%, attributed to optimized conjugation length.[10] However, our star-shaped HTMs provide advantages in dopant-free processing and stability, retaining more 90% of initial efficiency after 1200 hours (Fig. S2†), making them promising for practical applications. This comparison highlights the potential of star-shaped designs to balance efficiency and stability in PSCs.

Experimental

Materials

All solvents were purchased from Merck, Macklin or Acros Organics and used as received.

UV-vis absorption measurements

Absorption spectra for thin films deposited by spin-coating from 1×10^{-2} M solutions on quartz substrates were measured in UV-visible region (300–800 nm) on fiber optical spectrometer OPTOSKY ATP 2400.

Thermal properties

The thermal properties of the polymers were investigated by thermal gravimetry analysis using Thermal Analysis System TGA/DSC (Mettler Toledo) instrument under nitrogen with a heating rate of 10 °C min^{-1}. Differential scanning calorimetry was performed using Netzsch DSC 214 Polyma instrument at the same conditions.

Cyclic voltammetry measurements

Electrochemical measurements were carried out according to the previously reported method using an ELINS P-20-X instrument (Electrochemical Instruments, Russia), except of using chlorobenzene for deposition of all films.[42]

Hole mobility measurements

SCLC devices were fabricated on glass substrates with photolithographically defined bottom ITO electrode. PEDOT:PSS (PH 1000, Heraeus Clevios) was deposited by spin-coating. The substrates were subsequently dried at 160 °C for 10 min. Compounds HTMs were deposited by spin-coating from chloroform solutions giving film thicknesses in the range of 150–230 nm. After that, MoO_x and Ag were successively deposited by thermal evaporation in a vacuum chamber (6×10^{-6} mbar) to form the top electrode. The film thickness was recorded by making a thin scratch on the top of films. Subsequently, the AFM was scanned across the cut and the film thickness could thus be extracted from the resulting image.

Characterization of bilayer stacks

The steady-state PL and time-resolved PL measurements was performed with TCSPC time correlated single photon counter technique on Horiba QuantaMaster spectrofluorometer. The normalized PL decay curves are presented in a logarithmic scale.

Device fabrication

Prior to ETL deposition, glass/ITO substrates were cleaned with sonication in water, acetone, and isopropanol, dried in N_2 flow, then were put to an air plasma chamber at 50 W for 15 min. SnO_2 electron-transport layer was formed from 10% aqueous tin oxide (IV) colloidal dispersion using dynamic spin-coating at 4000 rpm for 30 s, and then annealed at 175 °C for 15 min. The hot substrates were transferred to inert (N_2) atmosphere of glovebox followed by annealing at 150 °C for 10 min. PCBA was deposited from 0.4 mg mL^{-1} chlorobenzene solution statically at 3000 rpm, then heated at 100 °C for 10 min. After that, the perovskite precursor (1.4 M MAI, 1.4 M PbI_2 in 4 : 1 DMF : NMP mixture) was deposited at 4000 rpm dynamically. The $MAPbI_3$

crystallization was triggered by the toluene (150 μL at 18 s) antisolvent dripping followed by the substrate rotating for 40 s. The samples were left to rest for 15 min. Black substrates were slowly heated up to 80 °C and annealed at this temperature for 5 min. The reference HTM PTAA was deposited from 6 mg mL^{-1} chlorobenzene solution at 4000 rpm for 15 s on cool substrates. The HTMs were deposited from preheated to 90 °C 7 mg mL^{-1} chlorobenzene solutions. The deposition conditions of all materials were optimized in preliminary experiments. Thicknesses of PTAA and HTLs were measured using AFM and are in the range of 15 ± 5 nm. The MoO_x (11 nm) and Ag (100 nm) layers were thermally evaporated under reduced pressure (10^{-5} mbar).

Device characterization

The efficiency of the devices was determined with the current–voltage (*J–V*) characterization under simulated 100 mW cm^2 AM 1.5G solar irradiation provided by the Newport Verasol AAA class solar simulator. The silicon diode with documented spectral response served as a standard for calibration. Current–voltage dependencies were record-ed under N_2 atmosphere using Kethley 2400 source-measurement unit. The active electrode area of the solar cells was defined with the 0.08 cm^2 shadow mask.

The EQE spectra were measured using QEXL External Quantum Efficiency Measurement System (USA) in an inert atmosphere.

The devices for stability investigation in unencapsulated devices (ITO/ZnO/MAI/PCBA/$CsFAPbI_3$/HTM/VO_x/Al) under continuous illumination in a glovebox, as reported previously.[43]

Conclusions

This study systematically investigated the potential of three novel small-molecule hole-transporting materials **DPAMes-TT**, **TPA-TT**, and **PhFF-TT** in perovskite solar cells (PSCs) with an n–i–p architecture. Through a detailed characterization of their optical, electrochemical, thermal, and charge transport properties, we elucidated the critical role of chemical structure in determining their performance. **DPAMes-TT** and **TPA-TT** featuring electron-donating conjugated core with bithiophene groups, exhibited favorable optical bandgaps, deep HOMO levels (−5.28 eV and −5.30 eV) aligned good with VB of $MAPbI_3$ and high hole mobilities (8.7×10^{-4} cm^2 V^{-1} s^{-1} and 2.7×10^{-4} cm^2 V^{-1} s^{-1}). These properties coupled with their H-aggregation tendencies facilitated efficient hole extraction, as evidenced by short TRPL lifetimes (*e.g.*, τ_1 = 9.3 ns for **DPAMes-TT**) and minimal interfacial recombination, leading to superior device performance with PCEs of 19.3% and 18.5%, respectively. Both materials outperformed the PTAA reference in solar cells (PCE 18.1%). In contrast, **PhFF-TT** with electron-withdrawing trifluorobenzene core displayed a wider bandgap (2.95 eV), a higher HOMO (−5.14 eV), and J-aggregation, resulting in poor charge transport (2.1×10^{-4} cm^2 V^{-1} s^{-1}), increased charge recombination (τ_2 = 91.1 ns), and defective interfaces that resulted in low FF (56.2%) and overall PCE of 12.6%.

These properties position **DPAMes-TT** and **TPA-TT** as promising candidates for cost-effective and scalable PSC fabrication, offering a viable alternative to conventional dopant-dependent HTMs like PTAA. Our findings demonstrate the significant influence of molecular structure on charge dynamics and device performance, providing a deeper understanding of structure-performance relationships in small-molecule HTMs. This study lays a foundation for future research, particularly in optimizing molecular structure to mitigate aggregation effects, such as those observed in **PhFF-TT**, to further enhance efficiency and scalability in PSC technology.

Data availability

The data for this article, The HTMs compound synthesis method, bi-exponential fit parameters TRPL, non-normalized PL of thin films, are available in the ESI.†

Author contributions

Investigation M. A., I. K., M. T.; formal analysis M. T., A. A., I. M.; writing—original draft preparation I. M; writing—review and editing, M. T., A. A, V. V.; supervision, V. V., A. A; funding acquisition. I. M.

Conflicts of interest

There are no conflicts to declare.

Acknowledgements

This work was funded by Russian Science Foundation within the project No. 23-73-01279, https://rscf.ru/project/23-73-01279. The synthesis of compounds was supported by the Ministry of Education and Science of the Russian Federation (project 125032604426-5).

References

1 M. A. Green, E. D. Dunlop, M. Yoshita, N. Kopidakis, K. Bothe, G. Siefer, X. Hao and J. Y. Jiang, *Prog. Photovolt.: Res. Appl.*, 2025, **33**, 3–15.
2 Interactive Best Research-Cell Efficiency Chart | Photovoltaic Research | NREL, https://www.nrel.gov/pv/interactive-cell-efficiency.html, (accessed 31 March 2025).
3 N. Li, X. Niu, Q. Chen and H. Zhou, *Chem. Soc. Rev.*, 2020, **49**, 8235–8286.
4 O. Almora, G. C. Bazan, C. I. Cabrera, L. A. Castriotta, S. Erten-Ela, K. Forberich, K. Fukuda, F. Guo, J. Hauch, A. W. Y. Ho-Baillie, T. J. Jacobsson, R. A. J. Janssen, T. Kirchartz, R. R. Lunt, X. Mathew, D. B. Mitzi, M. K. Nazeeruddin, J. Nelson, A. F. Nogueira, U. W. Paetzold, B. P. Rand, U. Rau, T. Someya, C. Sprau, L. Vaillant-Roca and C. J. Brabec, *Adv. Energy Mater.*, 2025, **15**, 2404386.
5 Y. Wang, L. Duan, M. Zhang, Z. Hameiri, X. Liu, Y. Bai and X. Hao, *Sol. RRL*, 2022, (6), 2200234.

6 G. Xie, L. Chen, J. Liu, J. Yu, H. Yin, H. Li, Y. Yang, A. Liang and Y. Chen, *J. Mater. Chem. C*, 2025, **13**, 2040–2057.
7 B. Yu, L. Zhang, J. Wu, K. Liu, H. Wu, J. Shi, Y. Luo, D. Li, Z. Bo and Q. Meng, *J. Mater. Chem. A*, 2020, **8**, 1417–1424.
8 Q. Liao, Y. Wang, X. Yao, M. Su, B. Li, H. Sun, J. Huang and X. Guo, *ACS Appl. Mater. Interfaces*, 2021, **13**, 16744–16753.
9 E. A. Komissarova, S. A. Kuklin, A. V. Maskaev, A. F. Latypova, P. M. Kuznetsov, N. A. Emelianov, S. L. Nikitenko, I. V. Martynov, I. E. Kuznetsov, A. V. Akkuratov, L. A. Frolova and P. A. Troshin, *Sustainable Energy Fuels*, 2022, **6**, 3542–3550.
10 F. M. Rombach, S. A. Haque and T. J. Macdonald, 2021, preprint, DOI: DOI: **10.1039/d1ee02095a**.
11 P. M. Kuznetsov, I. V. Martynov, I. S. Zhidkov, L. G. Gutsev, E. A. Komissarova, A. V. Maskaev, A. I. Kukharenko, F. A. Prudnov and P. A. Troshin, *J. Phys. Chem. B*, 2023, **127**, 6432–6439.
12 P. M. Kuznetsov, I. V. Martynov, I. S. Zhidkov, L. G. Gutsev, E. A. Khakina, E. N. Zakharchenko, N. A. Slesarenko, A. I. Kukharenko and P. A. Troshin, *J. Mater. Chem. A*, 2023, **11**, 9019–9028.
13 W. Li, W. Zhao, K. Li and X. Han, *J. Mater. Chem. C*, 2024, **12**, 1147–1176.
14 Y. Fu, C. Li, Y. Zhao and D. Cao, *Dyes Pigm.*, 2025, **235**, 112617.
15 H. D. Pham, T. C. J. Yang, S. M. Jain, G. J. Wilson and P. Sonar, *Adv. Energy Mater.*, 2020, **10**, 1903326.
16 W. Li, W. Zhao, K. Li and X. Han, *J. Mater. Chem. C*, 2024, **12**, 1147–1176.
17 P. Yan, D. Yang, H. Wang, S. Yang and Z. Ge, *Energy Environ. Sci.*, 2022, **15**, 3630–3669.
18 M. Stolterfoht, P. Caprioglio, C. M. Wolff, J. A. Márquez, J. Nordmann, S. Zhang, D. Rothhardt, U. Hörmann, Y. Amir, A. Redinger, L. Kegelmann, F. Zu, S. Albrecht, N. Koch, T. Kirchartz, M. Saliba, T. Unold and D. Neher, *Energy Environ. Sci.*, 2019, **12**, 2778–2788.
19 I. Gelmetti, N. F. Montcada, A. Pérez-Rodríguez, E. Barrena, C. Ocal, I. García-Benito, A. Molina-Ontoria, N. Martín, A. Vidal-Ferran and E. Palomares, *Energy Environ. Sci.*, 2019, **12**, 1309–1316.
20 G. Xie, L. Chen, J. Liu, J. Yu, H. Yin, H. Li, Y. Yang, A. Liang and Y. Chen, *J. Mater. Chem. C*, 2025, **13**, 2040–2057.
21 W. Wang, J. Zhou and W. Tang, *J. Mater. Chem. A*, 2022, **10**, 1150–1178.
22 I. E. Kuznetsov, A. A. Piryazev, A. F. Akhkiamova, M. E. Sideltsev, D. V. Anokhin, A. V. Lolaeva, M. V. Gapanovich, D. S. Zamoretskov, D. K. Sagdullina, M. V. Klyuev, D. A. Ivanov and A. V. Akkuratov, *ChemPhysChem*, 2023, (24), e202300310.
23 M. E. Sideltsev, A. A. Piryazev, A. F. Akhkiamova, M. V. Gapanovich, D. V. Anokhin, D. K. Sagdullina, A. S. Novikov, D. A. Ivanov and A. V. Akkuratov, *Phys. Status Solidi RRL*, 2024, (18), 2300223.
24 E. E. Agafonova, M. M. Tepliakova, D. O. Balakirev, I. V. Dyadishchev, P. K. Sukhorukova, A. N. Solodukhin, A. Elakshar, S. Y. Luchkin, A. M. Ionov, S. G. Protasova, A. V. Novikov, D. S. Zamoretskov, A. G. Nasibulin, A. V. Akkuratov and K. J. Stevenson, *Sol. Energy Mater. Sol. Cells*, 2023, **252**, 112168.
25 N. J. Hestand and F. C. Spano, *Chem. Rev.*, 2018, **118**, 7069–7163.
26 M. Li, A. H. Balawi, P. J. Leenaers, L. Ning, G. H. L. Heintges, T. Marszalek, W. Pisula, M. M. Wienk, S. C. J. Meskers, Y. Yi, F. Laquai and R. A. J. Janssen, *Nat. Commun.*, 2019, **10**, 2867.
27 A. Akkuratov, I. Martinov, I. Avilova and P. Troshin, *Phys. Status Solidi RRL*, 2019, **13**, 1900154.
28 Z. Xie, D. Liu, C. Gao, X. Zhang, H. Dong and W. Hu, *J. Am. Chem. Soc.*, 2025, **147**(3), 2239–2256.
29 C. M. Sullivan, A. M. Szucs, T. Siegrist and L. Nienhaus, *J. Phys. Chem. C*, 2024, **128**(45), 19248–19259.
30 C. M. Cardona, W. Li, A. E. Kaifer, D. Stockdale and G. C. Bazan, *Adv. Mater.*, 2011, **23**, 2367–2371.
31 S. Xiong, Z. Hou, S. Zou, X. Lu, J. Yang, T. Hao, Z. Zhou, J. Xu, Y. Zeng, W. Xiao, W. Dong, D. Li, X. Wang, Z. Hu, L. Sun, Y. Wu, X. Liu, L. Ding, Z. Sun, M. Fahlman and Q. Bao, *Joule*, 2021, **5**, 467–480.
32 A. Y. Alsalloum, B. Turedi, X. Zheng, S. Mitra, A. A. Zhumekenov, K. J. Lee, P. Maity, I. Gereige, A. AlSaggaf, I. S. Roqan, O. F. Mohammed and O. M. Bakr, *ACS Energy Lett.*, 2020, **5**, 657–662.
33 M. E. Sideltsev, A. N. Zhivchikova, I. E. Kuznetsov, D. K. Sagdullina, M. M. Tepliakova, A. A. Piryazev, D. V. Anokhin, M. S. Maksimovich, N. G. Nikitenko, D. A. Ivanov and A. V. Akkuratov, *Sustainable Energy Fuels*, 2024, **8**, 2437–2445.
34 I. V. Martynov, A. N. Zhivchikova, M. D. Tereshchenko, I. E. Kuznetsov, S. Baryshev, V. S. Volkov, M. Tepliakova, A. V. Akkuratov and A. V. Arsenin, *Sustainable Energy Fuels*, 2024, **8**, 3704–3710.
35 D. Jayan K and V. Sebastian, *Adv. Theory Simul.*, 2021, **4**, 2100027.
36 P. N. Murgatroyd, *J. Phys. D Appl. Phys.*, 1970, **3**, 308.
37 V. M. Le Corre, E. A. Duijnstee, O. El Tambouli, J. M. Ball, H. J. Snaith, J. Lim and L. J. A. Koster, *ACS Energy Lett.*, 2021, **6**, 1087–1094.
38 Y. Ko, Y. Kim, C. Lee, Y. Kim and Y. Jun, *ACS Appl. Mater. Interfaces*, 2018, **10**, 11633–11641.
39 C. Dreessen, L. Gil-Escrig, M. Hülsbeck, M. Sessolo, H. J. Bolink and T. Kirchartz, *Sol. RRL*, 2024, **8**, 2400504.
40 J.-P. Correa-Baena, W. Tress, K. Domanski, E. H. Anaraki, S.-H. Turren-Cruz, B. Roose, P. P. Boix, M. Grätzel, M. Saliba, A. Abate and A. Hagfeldt, *Energy Environ. Sci.*, 2017, **10**, 1207–1212.
41 Q. Cao, Y. Li, H. Zhang, J. Yang, J. Han, T. Xu, S. Wang, Z. Wang, B. Gao, J. Zhao, X. Li, X. Ma, S. M. Zakeeruddin, W. E. I. Sha, X. Li and M. Grätzel, *Sci. Adv.*, 2021, **7**, 28.
42 A. N. Mikheeva, I. E. Kuznetsov, M. M. Tepliakova, A. Elakshar, M. V. Gapanovich, Y. G. Gladush, E. O. Perepelitsina, M. E. Sideltsev, A. F. Akhkiamova, A. A. Piryazev, A. G. Nasibulin and A. V. Akkuratov, *Molecules*, 2022, **27**(23), 8333.
43 M. M. Tepliakova, A. N. Mikheeva, P. A. Somov, E. S. Statnik, A. M. Korsunsky and K. J. Stevenson, *Energies*, 2021, **14**, 5115.